Brain tumor detection through image fusion using enhanced dual channel pulse coupled neural networks and grey wolf optimizer

Ratna Kumari Jogi* , Usha Rani Macigi

Department of Computer Science, Sri Padmavati Mahila Vishwavidyalayam, Tirupati, Andhra Pradesh, India.

*Corresponding author: ratnakumarijogi@gmail.com

Abstract:

Image fusion is particularly crucial for diagnostic imaging in medical applications such as radiation therapy and image-guided surgeries. Medical image fusion seeks to improve diagnostic accuracy by preserving important characteristics and features from the individual pictures in the combined image. This study introduces a novel fusion methodology for MRI and CT medical imaging by decomposing the source images as base and detail layers using a novel three-scale decomposition strategy that employs Gaussian and Guided filters. Gaussian curvature directs the guided filtering procedure for each source image. The base layers are fused using the Proposed Grey Wolf Optimization algorithm (PGWO), which contains an objective function designed to maximize entropy, edge strength, and standard deviation. In order to integrate the detail layers, the activity level information is simultaneously determined using the Enhanced Dual Channel PCNN. To evaluate the effectiveness of the proposed method, thirty slices of seven different types of medical images from various sources were analyzed and compared both visually and statistically with existing approaches. According to experimental data, the suggested approach performs better than traditional approaches in terms of both objective metrics and qualitative image quality. Quantitative findings show notable advancements over current techniques: Standard deviation rises from 15.5 to 32.7%, spatial frequency from 38.2 to 70.5%, mutual information from 42.8 to 62.9%, edge strength from 37.4 to 61.9%, structural similarity index from 37.8 to 43.8%, and image entropy from 12 to 18%.

Keywords: Image fusion; Gaussian; Guided filter; Grey wolf optimization; Enhanced dual channel pulse coupled neural networks; Entropy; Edge strength and pixel intensity

1. Introduction

The rapid development of sensor technology has made it possible for many sensors to collect a wide variety of images. Multimodal biomedical imaging frequently uses techniques like Phase Contrast (PC) imaging, Magnetic Resonance Imaging (MRI), Positron Emission Tomography (PET), Single Photon Emission Computed Tomography (SPECT), Green Fluorescent Protein (GFP), and Computed Tomography (CT). Because MRI provides detailed cross-sectional, sagittal, coronal, and inclined-plane views of the human body, it can accurately localize lesions and provide a 3D representation of them. CT scans, which illustrate the way various organs and tissues absorb X-rays, show brighter areas for higher-density tissues, including bone. Thus, CT scans can be used to locate the dense tissues in the body. Radiation-based imaging methods such as PET and SPECT

detect varying amounts of tracer molecules that are injected into the bloodstream and correspond to varying levels of tissue activity. As a result, abnormal metabolic activity in tissues can be found and detected using PET and SPECT, which aids in the diagnosis of disorders. Two frequently used imaging methods in molecular biology are GFP and PC. Because PC imaging sheds light on the structural properties of cells, it can be used to detect subtle changes in cellular components such the mitochondria, cytoplasm, or nucleus. GFP imaging, on the other hand, shows the distribution of proteins. While PC images offer better grayscale spatial resolution, GFP images highlight the protein dispersion. The objective of PC-GFP image fusion is to combine these advantages by preserving the phase contrast image's structural features and making it possible to identify regions with high protein activity. This fusion enhances biomedical analysis

by providing detailed information and more accurate protein localization. However, a single sensor can only record one type of image. Image fusion produces a composite image with higher visual quality and more detailed information by combining images from various modalities. Therefore, image fusion is a very useful technique in many fields, including image retrieval and classification, computer-aided diagnostics, and object identification.

Despite the wide variety of fusion methodologies, most of them employ multiscale and multi-resolution transformation (MST-MRT) techniques. By applying different fusion rules to different layers, the fusion results can be improved, and MST-MRT-based algorithms can capture multiscale properties at different resolutions. Some of the MST-based techniques that have been introduced are Non-Subsampled Shearlet Transform (NSST) [1, 2], Non-Subsampled Contourlet Transform (NSCT) [3, 4], wavelet-based methods [5, 6], and pyramid-based approaches [7, 8]. Wavelet-based fusion methods extract multi-scale information using the wavelet transform, with adjustable fusion algorithms for wavelet coefficients. Following that, the inverse wavelet transform is applied to produce the fused image. Wavelet-based fusion approaches frequently produce fuzzy fused images because of the significant amount of detail lost during the process, even if they offer flexible decomposition utilizing various wavelet basis functions. Detail is also lost during the decomposition and fusing phases of pyramid-based fusion techniques. NSST and NSCT, which offer multi-scale and multi-directional transformations, are a more recent and rapid class of transformations. These methods allow fused images maintain their edges and details to some extent, even though high-frequency coefficient loss during the fusion process can still result in fuzzy edges and blurred features.

Another prominent fusion method is sparse representation (SR) [9], which consists of two main components: Dictionary learning and coefficient optimization. SR is quite versatile and can be applied to image denoising, information fusion, and restoration. However, there are several drawbacks to SR-based fusion methods. For example, selecting the appropriate dictionary size can be challenging; a vocabulary that is too large slows down the fusion process, while a dictionary that is too small produces incomplete information and less-than-ideal fusion results. Furthermore, because different methods produce varying fusion results, choosing the ideal optimization methodology might be difficult. Filter-based algorithms have gained popularity in imaging due to their efficiency and speed. The development of guided image filters in 2013 was a major advancement [10]. However, its ability to preserve edges and reduce noise is limited because it only considers spatial weights. The rolling guidance filter [11], which contains multiple guidance processes and considers both range and spatial weights, was proposed in 2014 in order to overcome these limitations. As a result, the rolling guidance filter can preserve large-scale architecture while eliminating minute details. In recent years, deep convolutional neural networks (CNNs) [12, 13] have gained popularity in applications linked to imaging. CNNs are composed of three main layers: convolution, pooling,

and activation. Once trained, CNNs can fit a large variety of data. They may be applied to a wide range of difficult tasks, including image fusion, classification, segmentation, and super-resolution, because to their versatility. Due to their self-attention mechanism, transformer-based models have quadratic complexity with regard to image size [14], which results in significant computational overhead even if they perform exceptionally well at global modeling. Additionally, when compared to CNNs, Transformers show less accuracy in capturing local features. Though some fusion models use a hybrid strategy that combines Transformer and convolutional layers to capitalize on their individual advantages and minimize their disadvantages, but computational expense is still a major concern [15, 16].

Recent years have seen the development of numerous meta-heuristic optimization strategies that have been effectively used to medical image fusion. Some significant examples include Quantum-behaved Particle Swarm Optimization [17], Modified Central Force Optimization [18], Gray Wolf Optimization [19], Chaotic Grey Wolf Optimization [20], Hybrid Genetic and Grey Wolf Optimization [21], Particle Swarm Optimization with Non-Subsampled Shearlet Transform [22], Binary Crow Search Optimization [23], Modified Shark Smell Optimization [24], and Particle Swarm Optimization-based cartoon-texture decomposition based on total variation [25]. There are some shortcomings with the current image fusion techniques. The first constraint is the low-frequency component fusion strategy, which uses a weighted average rule. The problem still exists in some contemporary techniques, including Two-Scale Structure Tensor Image Decomposition [26], Convolutional Sparse Representation [27], Morphological Component Analysis in Convolutional Sparsity [28], Sparse Representation in Two-Scale Image Decomposition [29], and Two-Scale Image Decomposition Using Sparse Representation and Guided Filtering [30]. This restriction results in a decrease in the intensity of composite image. The inadequate fusing of high-frequency coefficients is the second issue. Certain information is difficult to maintain using current approaches due to their low preservation indices. Local Variance [31], Max Selection [32], and Parameter-Adaptive Pulse Coupled Neural Network [33] are a few often utilized fusion rules. This could lead to the loss of important information in the fused image.

In this paper, we propose a novel approach that employs two algorithms to address these limitations. The key advantages of the recommended approach are outlined below:

1. The first method determines the optimal fused base layer settings using the Grey Wolf Optimization approach (GWO) to ensure that the fused image has improved contrast.

2. The second method efficiently preserves the detailed information of the input images in the fused image by using Enhanced Dual Channel PCNN to offer an effective fusion rule of the detail layers.

2. Background

2.1 Tri-scale image decomposition

There are numerous methods for splitting an image into two scales. These techniques have been applied to a number of medical image fusion approaches. A tri-scale image decomposition technique is presented in this paper. The suggested image decomposition technique is illustrated in figure 1. Here, a Gaussian filter is used to the input image to form the base layer, which consists of homogeneous areas of the image. An image is then passed through a guided filter, which employs the guidance image as Gaussian curvature of the source image, in order to extract the detail layers. The detail layer with significant variations is obtained by subtracting the Gaussian filter's output from the guided filter's output, and the detail layer with minute scale changes is obtained by subtracting the guided filter's output from the original image.

2.1.1 Algorithm of proposed tri-scale decomposition

Step 1: Let the input image to be decomposed is I_1.

Step 2: Base layer of I_1 is obtained is filtering it using Gaussian lowpass filter with $\sigma = 3$.

$$I_B = \text{Gaussian}(I_1, 3) \tag{1}$$

Where Gaussian function of 2D is defined as $I_1(x, y, \sigma) = \frac{1}{2\pi\sigma^2} \exp(-\frac{x^2+y^2}{2\sigma^2})$, with (x, y) representing the spatial co-ordinates of an image.

Step 3: Obtain the Gaussian curvature of input image as follows:

(a) Obtain the smoothed image of I_1 using equation (2)

$$I_s = \text{Gaussian}(I_1, 3) \tag{2}$$

(b) Compute the first order partial derivatives of I_s along x and y directions using equation (3) to get gradient.

$$I_x = \frac{\partial I_s}{\partial x} \quad \text{and} \quad I_y = \frac{\partial I_s}{\partial y} \tag{3}$$

(c) Compute the second order partial derivatives of I_s along x and y directions using equation (4)

$$I_{xx} = \frac{\partial^2 I_s}{\partial x^2} \quad \text{and} \quad I_{yy} = \frac{\partial^2 I_s}{\partial y^2} \quad \text{and} \quad I_{xy} = \frac{\partial^2 I_s}{\partial x \partial y} \tag{4}$$

(d) Compute Gaussian curvature (K) of an image using equation (5)

$$K = \frac{I_{xx}I_{yy} - I_{xy}^2}{(1 + I_x^2 + I_y^2)^2} \tag{5}$$

The denominator $(1 + I_x^2 + I_y^2)^2$ ensures that the curvature is scaled appropriately based on the gradients of the image.

Step 4: Obtain the Guided filtered image (I_G) of input image by taking Gaussian curvature (K) as guidance image.

$$I_G = \text{guided filter}(I_1, K, r, \varepsilon) \tag{6}$$

where r, ε are the size of neighborhood and regularization parameters of guided filter which are taken as 15 and 0.01.

Step 5: Compute the detail layer with small scale variations (I_{DS}) by subtracting the guided filtered image from original image.
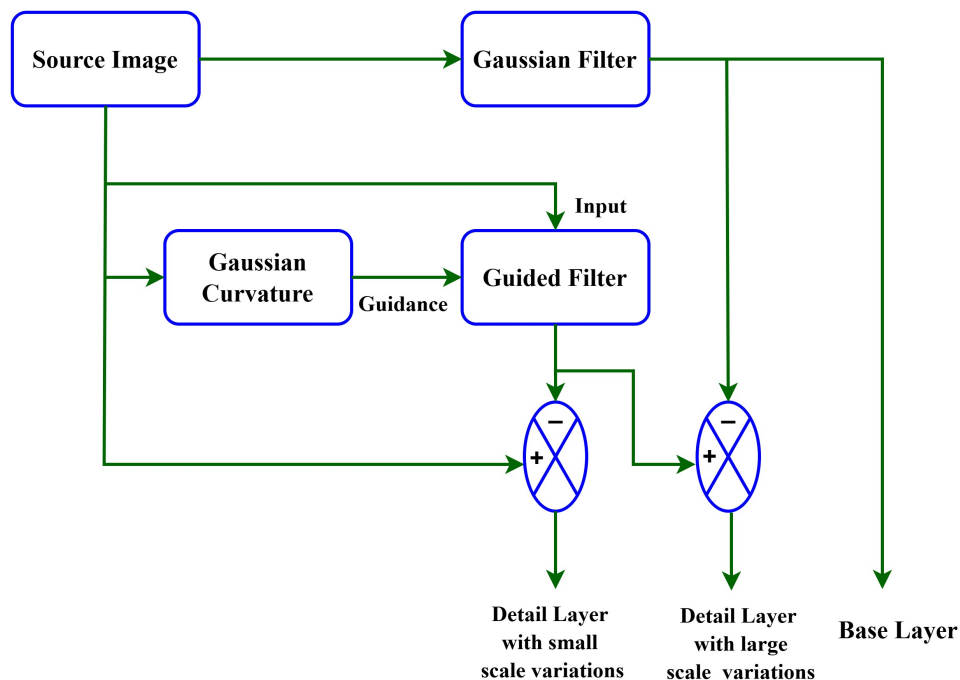
$$I_{DS} = I_1 - I_G \tag{7}$$

Figure 1. Proposed Tri-scale image decomposition model.

Step 6: Compute the detail layer with large scale variations (I_{DL}) by subtracting the Gaussian filtered image from guided filtered image.

$$I_{DL} = I_G - I_B \qquad (8)$$

The results of proposed novel tri-scale image decomposition technique are illustrated in figure 2.

2.2 Grey wolf optimization (GWO)

Gray wolf groups provide models for GWO through their social structure and foraging practices. A computer program simulates grey wolf tracking, surrounding, hunting, and attacking activities in order to maximize the population of gray wolves. Gray wolves forage in three stages: social hierarchy classification, encircling the prey, and attacking the prey [34].

2.2.1 Social hierarchy categorization:

Gray wolves are sociable canids with a rigid hierarchy of social dominance. The best solution (α) is highlighted, followed by the second-best (β) and third-best (δ). Other solutions are designated as ω as shown in figure 1.

2.2.2 Encircling the prey:

When hunting, gray wolves encircle their prey, which can be mathematically modeled using equations (9) to (12)

$$X(t+1) = X_p(t) - \mathbf{A} \times \mathbf{D} \qquad (9)$$

$$\mathbf{D} = |\mathbf{C} \times X_p(t) - X(t)| \qquad (10)$$

$$\mathbf{A} = 2a \times r_1 - a \qquad (11)$$

$$\mathbf{C} = 2 \times r_2 \qquad (12)$$

When t reflects the current iteration, X denotes the location vector associated with the gray wolf, and X_p represents the position vectors of the prey. $\mathbf{A}$ and $\mathbf{C}$ are coefficient vectors, r_1 and r_2 are random vectors in $[0,1]$, a is the distance controlling parameter, and its value falls linearly from 2 to 0.

2.2.3 Attacking the prey:

The search is primarily conducted under the direction of gray wolves, but they are also capable of identifying the location of possible prey. The top three wolves (α, β, δ) of the current population are retained in each iteration and the positions of the other search agents are then updated based on their position data. The mathematical modeling of this mechanism is described using equations (13) to (16).

$$X_1(t) = X_\alpha(t) - \mathbf{A}_1 \times \mathbf{D}_1 \qquad (13)$$

$$X_2(t) = X_\beta(t) - \mathbf{A}_2 \times \mathbf{D}_2 \qquad (14)$$

$$X_3(t) = X_\delta(t) - \mathbf{A}_3 \times \mathbf{D}_3 \qquad (15)$$

where

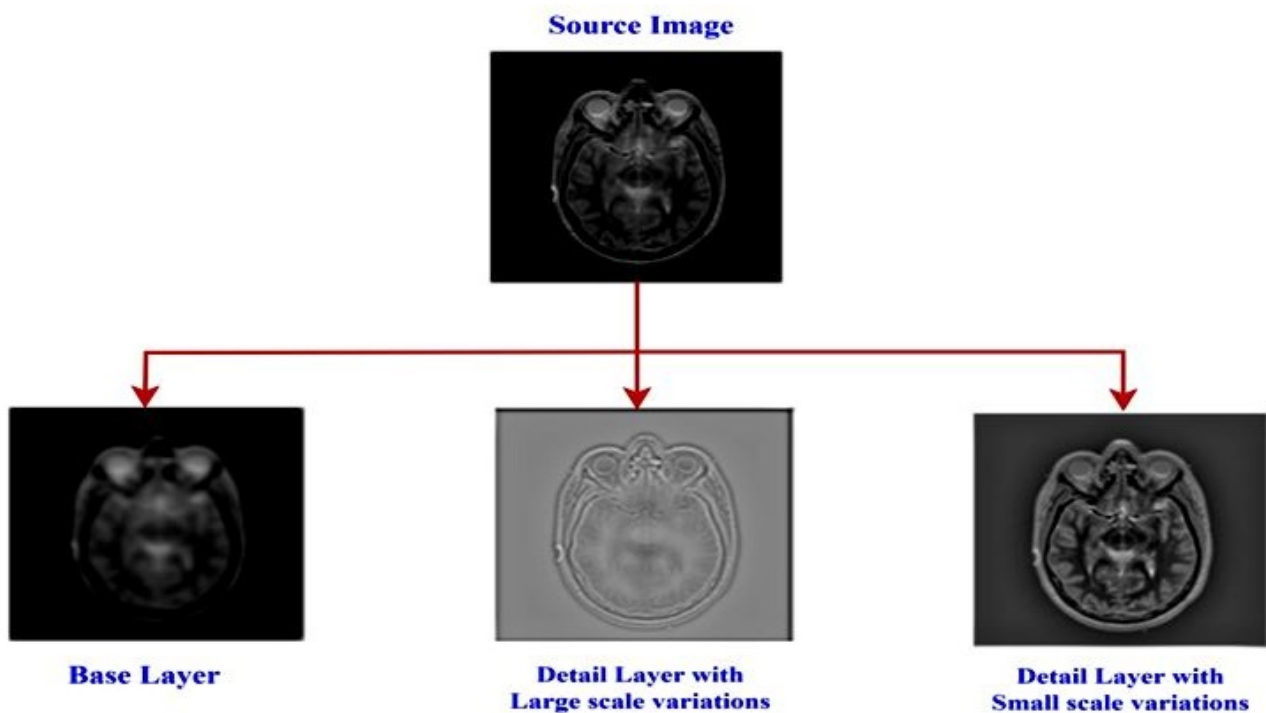$$\mathbf{D}_1 = |(\mathbf{C}_1)X_\alpha(t) - X(t)|$$

$$\mathbf{D}_2 = |(\mathbf{C}_2)X_\beta(t) - X(t)|$$

$$\mathbf{D}_3 = |(\mathbf{C}_3)X_\delta(t) - X(t)|$$

$$X(t+1) = \frac{X_1(t) + X_2(t) + X_3(t)}{3} \qquad (16)$$

In the above relations, X_α, X_β, X_δ signifies the location vectors of α, β and δ wolves respectively. The computations of $\mathbf{A}_1$, $\mathbf{A}_2$, and $\mathbf{A}_3$ like those of $\mathbf{A}$, and the numerical calculations of $\mathbf{C}_1$, $\mathbf{C}_2$, and $\mathbf{C}_3$ resemble those of $\mathbf{C}$. Instead of averaging $X_1(t)$, $X_2(t)$, and $X_3(t)$ to get updated

Figure 2. An example of proposed tri-scale image decomposition.

solution, the modified solution in Proposed Grey wolf optimization (PGWO) has two possible choices with each having equal probability to take place as illustrated in equation (17) and could provide better diversity of population.

$$X(t+1) = \begin{cases} \frac{(X_1(t)+X_2(t))}{2} & \text{if } p < 0.5 \\ \\ \frac{X_1(t)+X_2(t)+X_3(t)}{3} & \text{if } p \geq 0.5 \end{cases} \quad (17)$$

where p is an uniform random number in the interval $[0,1]$ generated new for each search agent.

3. Proposed fusion approach

In this section, we suggest two novel algorithms. The first one is suggested to combine detail layers based on proposed Enhanced Dual Channel Pulse Coupled Neural Network (EDPCNN) model. The second algorithm uses the tri-scale image decomposition method and the proposed Grey Wolf Optimization Algorithm to combine medical images.

3.1 Enhanced Dual Channel Pulse Coupled Neural Network (EDPCNN) model

Since the pixels with the highest activity are chosen for the fused output, it is essential to precisely determine the activity level of the related pixels in the original images while performing image fusion. An Enhanced Dual Channel Pulse Coupled Neural Network (EDPCNN) model is used in this study to assess the activity levels of detail layers. The firing module, data fusion block, and receptive field are the three main parts of the EDPCNN architecture, as seen in figure 3. Through their respective feeding inputs, F^I and F^J, the receptive field collects external stimuli for the two input images, I and J. Additionally, it gets a linking input L, from neighboring neurons. This is illustrated mathematically by using equation (18).

$$L_n(p,q) = \sum_{i=-1}^{1} \sum_{j=-1}^{1} W_s(i+2,j+2)Y_{n-1}(p+i,q+j) \quad (18)$$
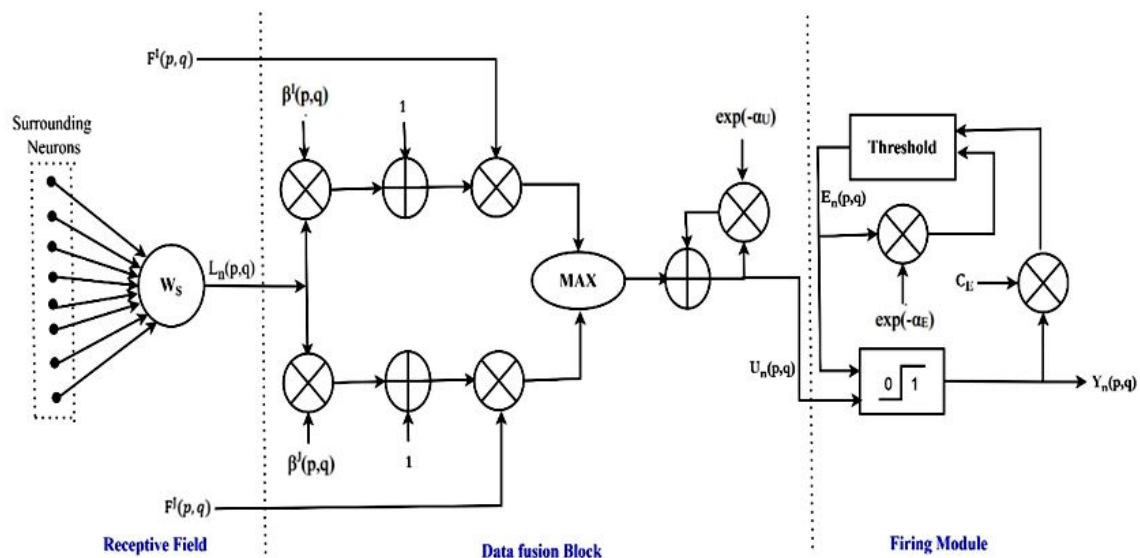
Here, the external inputs that correspond to images I and J are denoted by F^I and F^J, respectively. These inputs are continuously sent into the network for every iteration.

Spatial location of a neuron is indicated by (p,q), and the variable n denotes the number of iterations; each neuron corresponds to a pixel in the input images. The values of the surrounding pixels affect a pixel's significance in image processing. As a result, each neuron's linking input is determined by adding the weighted binary outputs of its nearby neurons from the previous iteration. The weight matrix W_s is a 3×3 matrix that allocates weights to nearby neurons according to their separation from the center neuron, while the binary output matrix is represented by Y.

$$W_s = \begin{bmatrix} \frac{1}{\sqrt{2}} & 1 & \frac{1}{\sqrt{2}} \\ 1 & 0 & 1 \\ \frac{1}{\sqrt{2}} & 1 & \frac{1}{\sqrt{2}} \end{bmatrix} \quad (19)$$

The data fusion block estimates the internal activity, represented by U, of the EDPCNN model in order to combine the complimentary data from both input images. Using equation (20), the internal activity for a specific iteration is calculated.

$$U_n(p,q) = e^{-\alpha_U} U_{n-1}(p,q) + \max\{U_n^I(p,q), U_n^J(p,q)\} \quad (20)$$

where U_n^I and U_n^J are the internal activities that correspond to the inputs F^I and F^J, respectively, at the nth iteration, and α_U is the exponential decay constant of U. Equations (21) and (22), which linearly modulates the feeding and connecting inputs, is used to compute these activities. Since neurons with higher internal activity tend to capture more prominent information, the input with the largest internal activity is usually selected for the fused image. To make it easier to integrate complementary information, a decay factor is included to the internal activity.

$$U_n^I(p,q) = F_n^I(p,q)(1 + \beta^I(p,q)L_n(p,q)) \quad (21)$$

$$U_n^J(p,q) = F_n^J(p,q)(1 + \beta^J(p,q)L_n(p,q)) \quad (22)$$

Figure 3. Enhanced Dual Channel Pulse Coupled Neural Network (EDPCNN) model.

Depending on the input images, β^I and β^J are adaptive connecting strengths. To build a robust linking strength, the eight-neighborhood modified Laplacian (EML) operator is utilized, which combines diagonal coefficients with neighborhood information. The EML [35] for $F^X|X \in (I,J)$ is calculated as follows:

$$
\begin{aligned}
EML^X(p,q) = &\;|F^X(p,q) - F^X(p,q-1)| \\
&+ |F^X(p,q) - F^X(p,q+1)| \\
&+ |F^X(p,q) - F^X(p-1,q)| \\
&+ |F^X(p,q) - F^X(p+1,q)| \\
&+ \frac{1}{\sqrt{2}}|F^X(p,q) - F^X(p-1,q-1)| \\
&+ \frac{1}{\sqrt{2}}|F^X(p,q) - F^X(p-1,q+1)| \\
&+ \frac{1}{\sqrt{2}}|F^X(p,q) - F^X(p+1,q-1)| \\
&+ \frac{1}{\sqrt{2}}|F^X(p,q) - F^X(p+1,q+1)|
\end{aligned}
\tag{23}
$$

The EML^X is smoothed using an averaging filter to reduce noise, producing an averaged EML ($AEML^X$). Then, by giving the pixels weights, the weighted EML ($WEML^X$) is obtained from $AEML^X$, where the central pixel is given the highest weight.

$$
WEML^X(p,q) = \sum_{i=-1}^{1}\sum_{j=-1}^{1} W_E(i+2, j+2) \\
\times \sqrt{AEML^X(p+i, q+j)}
\tag{24}
$$

where W_E is the weight matrix

$$
W_E = \frac{1}{16}\begin{bmatrix} 1 & 2 & 1 \\ 2 & 4 & 2 \\ 1 & 2 & 1 \end{bmatrix}
\tag{25}
$$

To operate with smaller values, this model uses $\sqrt{AEML^X}$ rather than $AEML^X$. Equation (14) is used to calculate the connecting strength of EDPCNN model, β^X. Since various pixels represent different kinds of information, variable connection strength is used.

$$
\beta^X(p,q) = WEML^X(p,q)
\tag{26}
$$

When neurons surpass their threshold, the firing module produces pulses, and equation (27) is used to calculate the binary output Y. When internal activity exceeds the threshold, a neuron fires and outputs a value of 1; if not, it outputs 0.

$$
Y_n(p,q) = \begin{cases} 1 & \text{if } U_n(p,q) > E_{n-1}(p,q) \\ 0 & \text{otherwise} \end{cases}
\tag{27}
$$

The threshold function, E, is adjusted according to equation (28)

$$
E_n(p,q) = e^{-\alpha_E}E_{n-1}(p,q) + C_E Y_n(p,q)
\tag{28}
$$

where α_E is the exponential decay constant for the threshold E and C_E is the amplitude constant. The threshold rises dramatically when a neuron activates, then progressively decreases till the neuron fires once again. In this study, $\alpha_E = 0.7$, $\alpha_E = 0.2$ and $C_E = 20$ is chosen based on information from literature [12, 13] in which similar models were used for image fusion.

3.2 Fusion of detail layers using EDPCNN

Here, the fused detail images are produced by using the internal dynamics of the inputs in the suggested EDPCNN model. The following settings are used to initialize the EDPCNN model for each detail layer I_{D1} and I_{D2} of the input images.

$$
\begin{aligned}
F^I(p,q) &= |I_{D1}| \\
F^J(p,q) &= |I_{D2}| \\
U_0(p,q) &= 0 \\
Y_0(p,q) &= 0 \\
E_0(p,q) &= 1
\end{aligned}
$$

Equation (26) is utilized to compute the parameter $\beta^X|X \in (I,J)$, and α_U is assigned based on the correlation between the EDPCNN model and the spiking cortical model [36]. The values for α_E and C_E are selected based on knowledge from previous research [37, 38]. The following are the specific values EDPCNN model.

$$
\alpha_U = 0.7,\; \alpha_E = 0.2 \;\text{ and }\; C_E = 20
$$

The EDPCNN model is simulated for N iterations after it has been configured, with N being set to 120. The fused detail layer I_{DF} is then calculated using the internal activities of the inputs, represented as I_{D1} and I_{D2}. Suppose that $U_N^{I_{D1}}(p,q)$ and $U_N^{I_{D2}}(p,q)$ indicate the internal activity of the input I_{D1} and I_{D2} respectively for the EDPCNN model at the $(p,q)^{\text{th}}$ neuron following the $N^{\text{thiteration}}$. The following equation is used to calculate the fused detail image.

$$
I_{DF}(p,q) = \begin{cases} I_{D1}(p,q) & \text{if } U_N^{I_{D1}}(p,q) \geq U_N^{I_{D2}}(p,q) \\ I_{D2}(p,q) & \text{if } U_N^{I_{D1}}(p,q) < U_N^{I_{D2}}(p,q) \end{cases}
\tag{29}
$$

3.3 Proposed algorithm based on Tri-scale decomposition and GWO

The proposed approach of image fusion is illustrated in figure 4 and it contain following steps:

Step 1: Read Input images I_1 and I_2 that needs to be fused

Step 2: Apply proposed tri-scale decomposition mechanism and decompose the source images into base layers (I_{B1} and I_{B2}), detail layers with significant variations (I_{DL1} and I_{DL2}) and detail layers with small scale variations (I_{DS1} and I_{DS2}).

Step 3: Fuse the detail layers using proposed fusion rule based on EDPCNN.

$$
D_a = \text{EDPCNN}(I_{DS1}, I_{DS2})
\tag{30}
$$

$$
D_b = \text{EDPCNN}(I_{DL1}, I_{DL2})
\tag{31}
$$
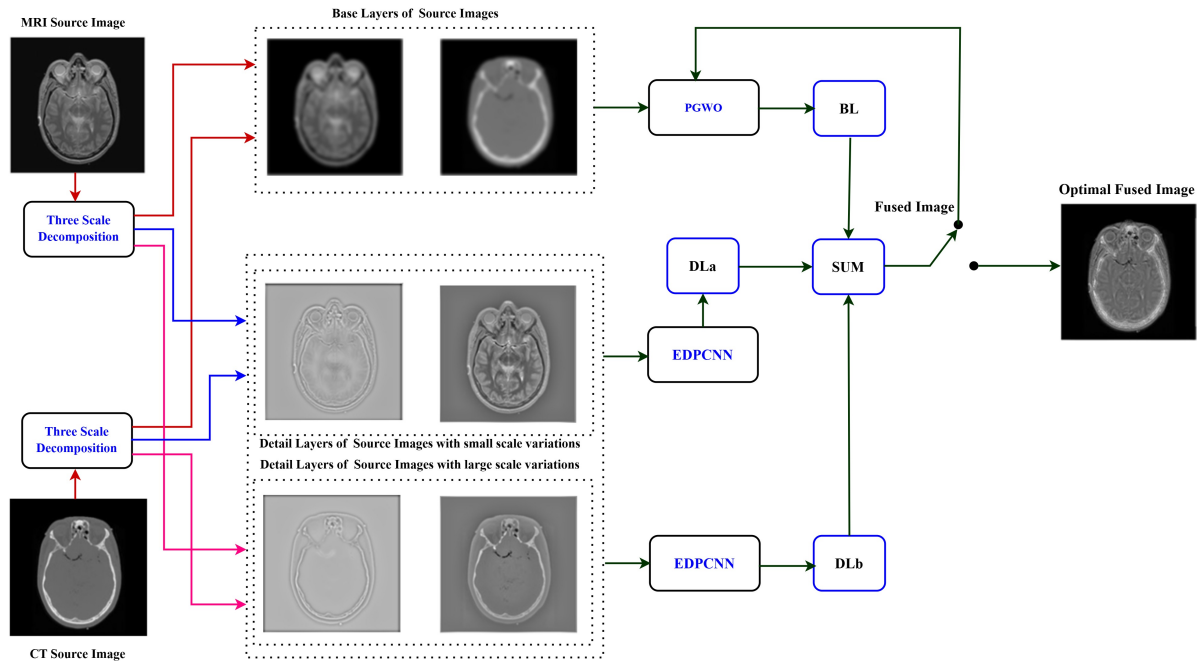
Figure 4. Proposed mechanism of image fusion for CT-MRI images.

Step 4: The base layer fusion is performed using a linear combination of two base layers, controlled by the fusion parameter $\beta \in [0, 1]$ which will be optimized.

$$\text{Fused base layer}, \ I_{Bf} = \beta \times I_{B1} + (1-\beta) \times I_{B2} \quad (32)$$

Step 5: Combining the fused based layer and the fused detail layers yields the final fused image.

$$\text{Fused Image}, \ I_{\text{fused}} = I_{Bf} + D_a + D_b \quad (33)$$

Step 6: Objective function is modeled as weighted sum of edge strength, entropy and mean pixel intensity and is used as maximization problem.

$$\begin{aligned}\text{Objective function, OF} = {} & \beta_1 \times E_{\text{edge}}(I_{\text{fused}}) \\ & + \beta_2 \times H(I_{\text{fused}}) \qquad (34) \\ & + \beta_3 \times \text{SD}(I_{\text{fused}})\end{aligned}$$

where E_{edge} (I_{fused}) indicates the edge strength of fused image and is calculated using the Laplacian filter. It is defined as the accumulation of the absolute values of the Laplacian-filtered image.

$$E_{\text{edge}}(I_{\text{fused}}) = \sum_i \sum_j |L(I_{\text{fused}}(i,j))| \quad (35)$$

where (i, j)-coordinates of pixels of an image.
$H(I_{\text{fused}})$ - Indicates entropy, which measures information content in an image. For an image with probability of pixel intensity distribution P_k, $H(I_{\text{fused}})$ can be calculated using equation (36).

$$H(I_{\text{fused}}) = -\sum_{k=0}^{255} P_k \log(P_k) \quad (36)$$

$\text{SD}(I_{\text{fused}})$- Indicates the standard deviation of the fused image. For a 256×256 image, $M = 256$ and $N = 256$ and $\text{SD}(I_{\text{fused}})$ is computed using equation (37).

$$\text{SD} = \sqrt{\frac{1}{MN} \sum_{i-1}^{M} \sum_{j=1}^{N} (f(i,j) - \mu)^2} \quad (37)$$

where $\mu = \frac{1}{MN} \sum_{i=1}^{M} \sum_{j=1}^{N} f(i,j)$.
β_1, β_2 and β_3 are the weighting factors of edge strength, entropy and standard deviation of fused image. Choosing appropriate values for the weights β_1, β_2 and β_3 in the objective function depends on the specific requirements and characteristics of the image fusion task. If the primary goal is to preserve the sharpness, structural details, and boundaries (e.g., in medical or satellite images), edge strength should be prioritized. In this case, β_1 is assigned higher value. If the objective is to maximize information content or contrast (e.g., for high-contrast imaging tasks), then entropy should have more influence. Increasing β_2 will help emphasize contrast and fine details. To have an image with more brightness, β_3 is assigned more value. In this work, values of β_1, β_2 and β_3 are taken as 0.4, 0.3, 0.3 respectively.

Step 7: The objective function is used to guide the GWO in finding the optimal fusion parameter (β), ensuring the maximization of edge strength, entropy, and standard deviation.

$$\beta_{\text{optimal}} = \text{argmax}(\text{OF}(\beta)) \quad (38)$$

Step 8: Using the β_{optimal}, Fused base layer relation of equation (32) is modified as follows:

$$I_{Bf \text{ optimal}} = \beta_{\text{optimal}} \times I_{B1} + (1 - \beta_{\text{optimal}}) \times I_{B2} \quad (39)$$

Step 9: From the optimal fused base layer, Optimal fused image is obtained using equation (40).

$$\text{Fused Image, } I_{\text{fusedoptimal}} = I_{Bf\text{optimal}} + D_a + D_b \quad (40)$$

In case of PET/SPECT source images, they are first converted from RGB color space to HIS color space and Intensity channel 'I' is used for fusion process. Once fused image is obtained, Hue (H) and Saturation channels of source image are used to obtain fused RGB image by performing HIS to RGB color space conversion. The detailed flow diagram of fusion process is illustrated in figure 5.

# 4. Results and discussion

4.1 Subjective analysis

A brain imaging-related PET-SPECT dataset and five MRI and CT datasets, referred to as "Dataset-I" through "Dataset-VII," were selected to evaluate the effectiveness of the proposed image fusion method. These include images of a healthy brain (Dataset-I), a brain with cerebellar metastases (Dataset-V), a brain that has had a fatal hemorrhage (Dataset-II), a brain that has been damaged by neoplastic cancer (Dataset-III), and sagittal brain and skull images (Dataset-IV). Additional analysis was done on the SPECT and MR-T2 datasets related to Metastatic Bronchogenic Disease (Dataset-VI) and the MR-T2 and PET datasets related to Alzheimer's disease (Dataset-VII). There are 256 grayscale levels and 256×256 pixels in each image. [http://www.med.harvard.edu/aanlib/home.html [39]]. The datasets are sourced from the Benchmark Brain Atlas. Figure 7 shows the fusion outcomes for Dataset-I, while Figs. 6 (a) and (b) show the original CT and MRI images, respectively. The results of fusion using a range of strategies, including the recommended method, Convolutional Neural Network (CNN), Non-Subsampled Shearlet Transform

(NSST), guided filter, Sparse Representation (SR), Discrete Wavelet Transform (DWT), and Convolutional Neural Network (CNN), are displayed in figure 6 (c) through (h) [40]. While skeletal structure is generally preserved in CT and connective tissue details in MRI, there are minor variations in contrast and detail preservation among the different modalities. These changes, particularly in the highlighted area, are shown by a yellow rectangle. The fused pictures in Figs. 6 (c) and (d) exhibit dim brightness in the highlighted area. While CNN and NSST fusion images successfully retain CT details (Figs. 6 (f) and (g)), MRI image information is often lost. Even though the guided filter produces visually clear results that are comparable to the recommended approach, the contrast is less, as seen in Figs. 6 (e) and 6(h). According to results of Dataset-II, which depicts a brain afflicted by a fatal hemorrhage, DWT and SR-based approaches perform poorly because to low contrast and a restricted ability to record bony structures and hemorrhagic severity, as seen in figure 7. While GFF and CNN provide substantial visual improvements, they sometimes lose essential pathological information. The suggested methodology, while significantly limited in its ability to preserve very tiny CT pixel intensity variations along row and column wise, maintains a better balance of contrast and structural accuracy than existing methods. Dataset-III, which represents a brain with neoplastic pathology, shows a dramatic disparity in performance as illustrated in figure 8. While standard approaches such as DWT, SR, and NSST fail to capture the full extent of soft tissue deformation induced by tumors, the suggested method excels at providing high contrast while preserving sensitive soft tissue features. This is especially important in clinical settings where tumor boundaries and penetration zones must be precisely defined.

Dataset-IV focuses on fusing MRI and CT scans of the brain and skull in sagittal perspectives. This dataset poses a unique challenge since it necessitates the integration of
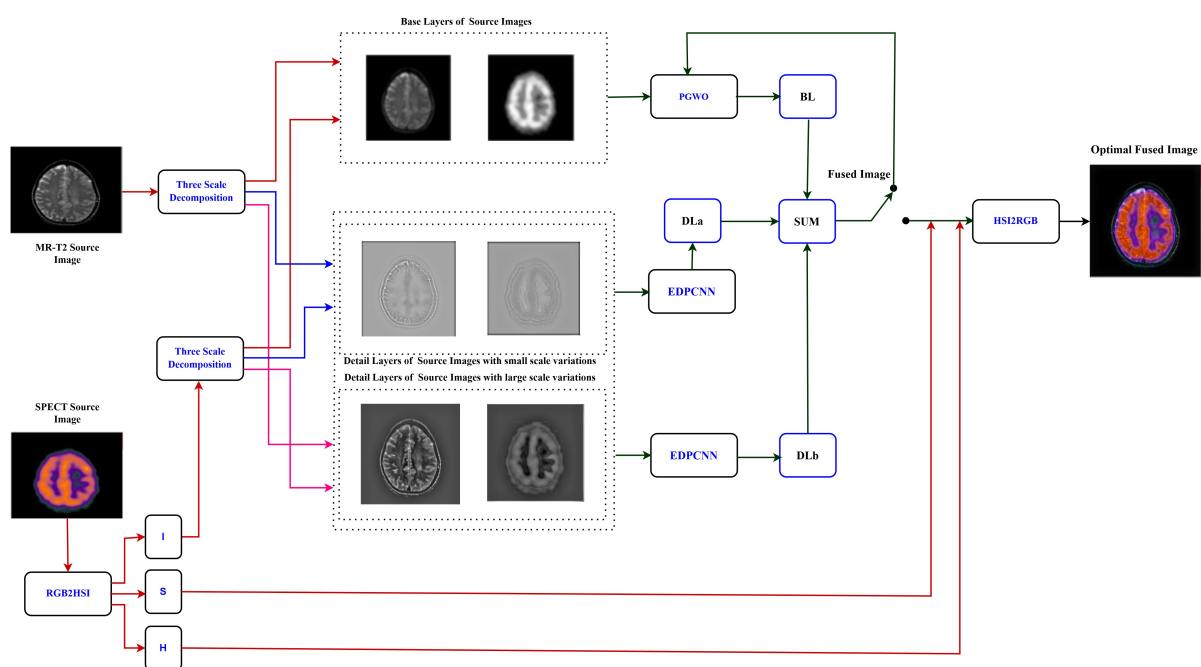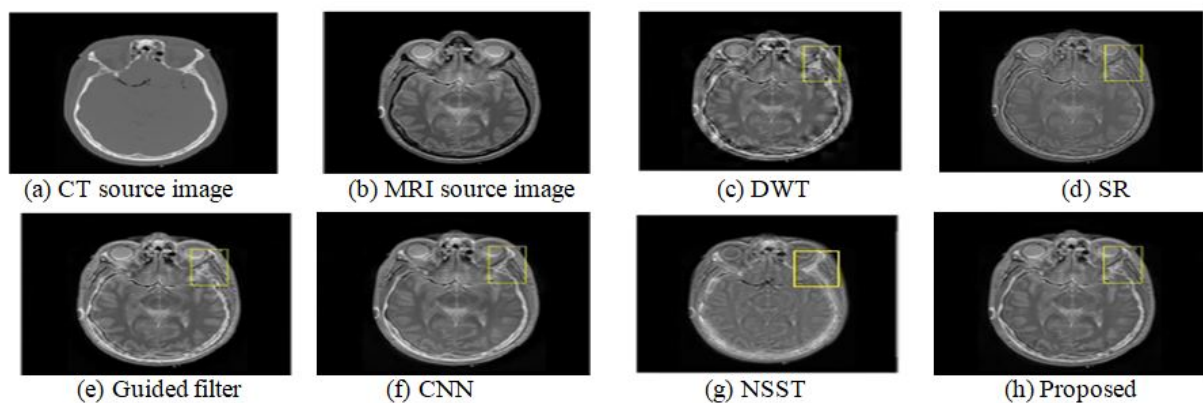

Figure 5. Proposed mechanism of image fusion for MR_T2 and PET/SPECT images.
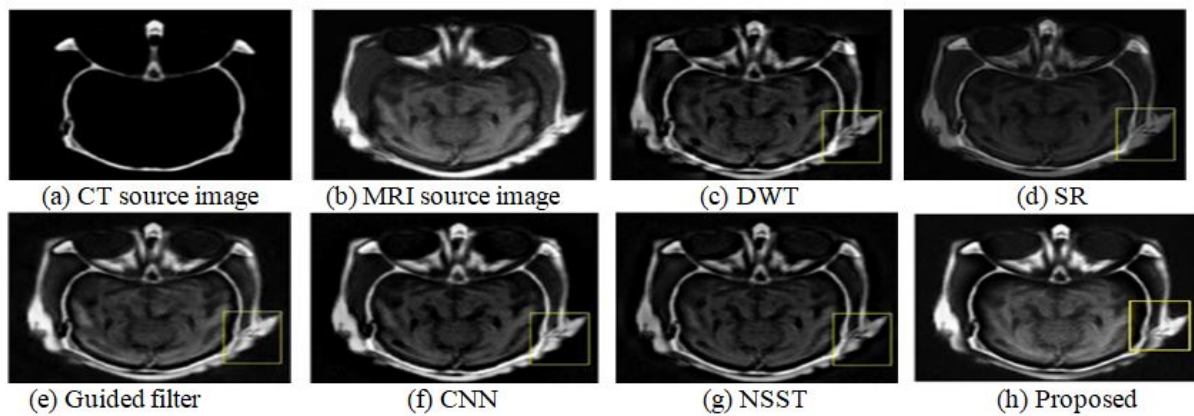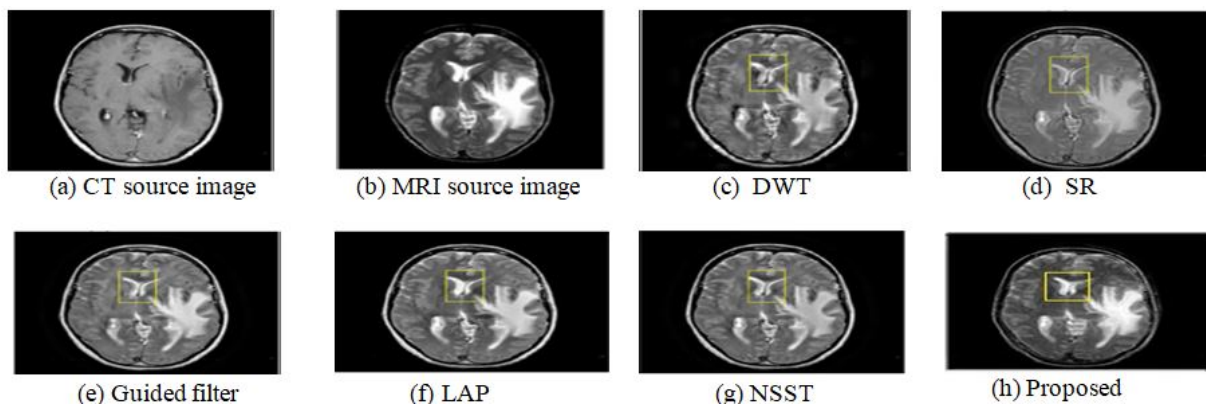
Figure 6. Fused images of Dataset-I (MRI-CT of healthy brain).

Figure 7. Fused images of Dataset-II (MRI-CT of Fatal stroke).


**Figure 8.** Fused images of Dataset-III (CT-MRI of neoplastic tumor).

complementary structural features—bony anatomy from CT and soft tissue contrast from an MRI. Traditional approaches, such as DWT and SR, fail in this situation. They fail to retain the fine details of the cranial bones, as illustrated in Figs. 9 (c) and 9 (d), resulting in blurred edges and poor anatomical clarity. Although the guided filter improves soft tissue visibility significantly, it ignores high-frequency components such as crisp skull outlines. CNN and NSST generate high contrast images while suppressing subtle MRI characteristics. In contrast, the proposed approach successfully maintains both the detailed bone features of CT and the subtle brain textures of MRI. The fused image in figure 9 (h) has sharp edges, smooth grayscale transitions, and

a well-balanced representation of both modalities. This highlights the ability of proposed algorithm to retain critical clinical data, making it useful in neurological and cranial examinations.

Dataset-V consists of the fusion of MRI and CT images from a brain impacted by Cerebella metastases. This information is especially important since it highlights structural deformations induced by metastatic lesions as well as the surrounding bone structure. As illustrated in Figs. 10 (c) and 10 (d), the DWT and SR approaches have limitations; they produce images with poor contrast and insufficient clarity in tumor-affected regions. Although NSST and guided filter approaches improve visual appearance, they do not capture
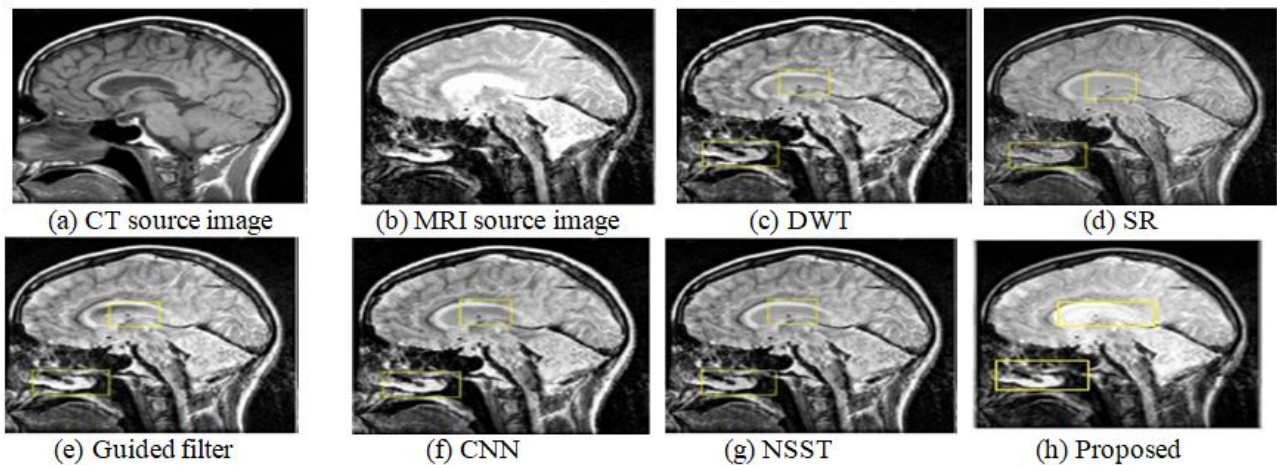
Figure 9. Fused images of Dataset-IV (MRI-CT of brain skull).
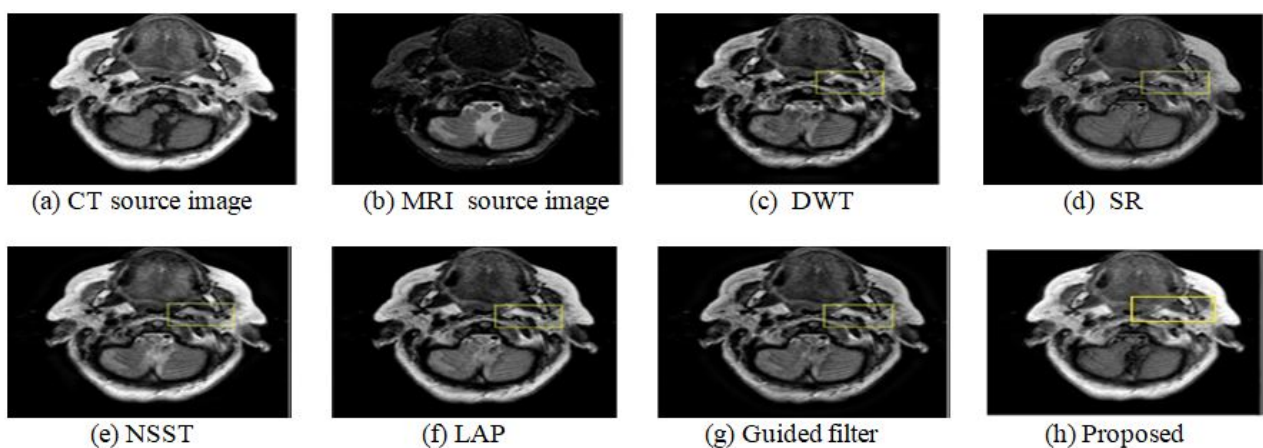
Figure 10. Fused images of Dataset-V (MRI-CT of Cerebella metastasis).

the full degree of lesion-induced changes in soft tissue. The CNN-based technique improves texture but adds slight artifacts that may complicate clinical interpretation. The suggested technique, illustrated in Fig. 10 (h), produces a balanced fusion output with increased contrast, well-preserved lesion boundaries, and detailed bone features. It successfully highlights the metastatic location while maintaining anatomical integrity. This feature is especially important for pre-operative planning and radiological evaluations, which need accurate visibility of tumor boundaries and surrounding anatomical structures.

In figure 11, MR-T2 and SPECT-TC images of metastatic bronchogenic lesions are combined. For the purpose of clarity, segmented portions of the photographs are displayed independently. The Guided Filter Fusion (GFF) approach does not preserve the original colors, and the Discrete Wavelet Transform (DWT) approach provides too little contrast. Despite their capacity to provide high contrast, the NSST and SR methods fall short in maintaining the structural integrity of the MR-T2 image. By successfully preserving the energy, structural, and color components of the source images, the proposed approach ensures superior fusion quality. Figure 12 displays a patient with intermediate-stage Alzheimer's disease whose PET and MR-T2 scans were fused. To improve visibility, segmented pieces are

displayed independently. Similar to the last dataset, DWT offers little contrast, however GFF struggles to maintain the original hues. CNN and SR techniques successfully restore the image attributes, however they do not retain the original colors. Additionally, the NSST method over-enhances the image, taking away from its natural look. On the other hand, the proposed technique successfully preserves crucial color and structural information while maintaining the uniqueness of the fused image, resulting in a balanced and visually accurate representation.

4.2 Objective analysis

To measure fusion performance, evaluation criteria that are qualitative as well as quantitative must be applied. In this paper, various fusion processes are assessed for their effectiveness using quantitative assessment measures such as standard deviation (SD), mutual information (MI), image entropy (IE), spatial frequency (SF), mean structural similarity (MSSIM), and margin information retention (QAB/F). Table 1 presents an explanation of these measurements.

Table 2 displays the quantitative analysis of image evaluation measures, with bold indicating the best-performing results. Measures such as Mutual Information (MI), Image Entropy (IE), QAB/F, and MSSIM all significantly improve with the proposed fusion procedure. These results show
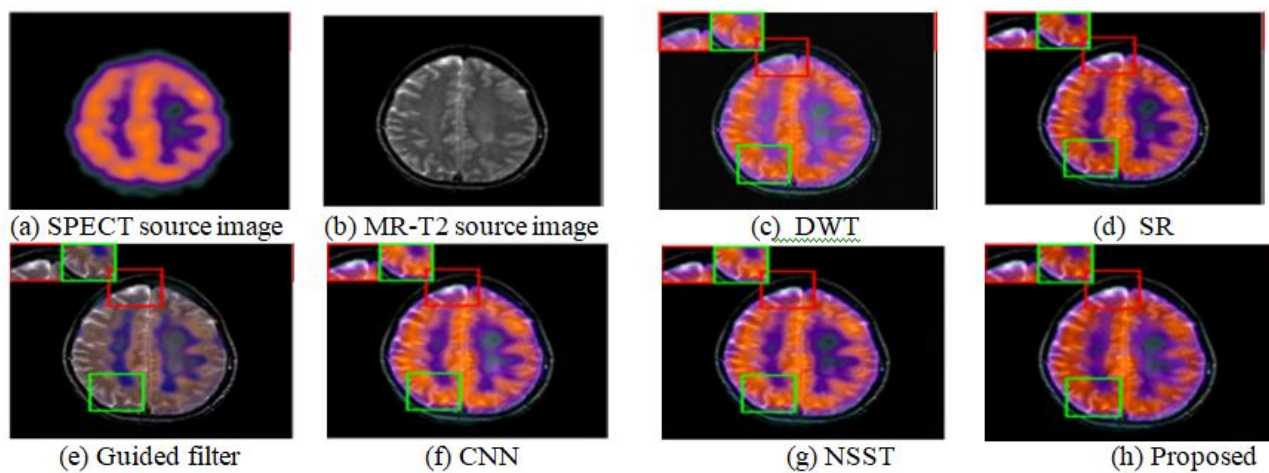
Figure 11. Fused images of SPECT and MR-T2 of Metastatic Bronchogenic.
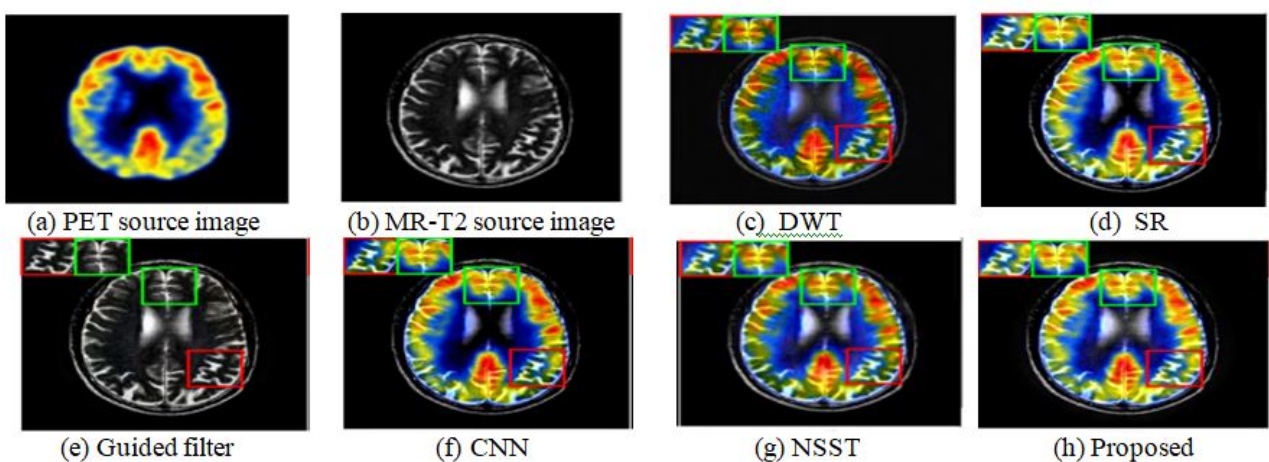
Figure 12. Fused images of PET and MR-T2 of Alzheimer's disease.

how well the suggested approach preserves edge characteristics and saliency information. For other criteria, the performance of the proposed strategy is comparable to existing methods. Figure 13 provides a visual comparison of alternative methods based on the average values of four key assessment metrics-MI, IE, MSSIM, and QAB/F—analyzed over thirty different datasets. This comparison shows how effectively the recommended method maintains significant image quality and characteristics.

4.3 Result analysis

The experimental data indicates that low intensity and a lack of knowledge about bone structure are the main causes of poor fusion results in Sparse Representation (SR) and DWT techniques. While methods such as NSST, CNN, and the guided filter perform visually well, they cannot fully preserve edge and texture details in the yellow-marked MR-CT fusion zones. Moreover, the Guided filter approach loses color fidelity in MR-SPECT and MR-PET fusion scenarios. The recommended method, on the other hand, effectively preserves crucial features, enhancing the depiction of soft tissues and bone structures and producing merged images that are clearer and more vibrant. The quality of fused images was assessed using six metrics, including image

entropy (IE), standard deviation (SD), and spatial frequency (SF), which are commonly used to assess intrinsic image properties. SF ensures that the image appears sharp, IE indicates the information content of the fused image, and SD measures contrast by examining the distribution of grey levels. Higher SD values suggest greater contrast, which facilitates the visualization of the fused image. By including extraneous elements, some modern methods exaggerate these measurements. Three more metrics-MI, MSSIM, and QAB/F are included in this paper for a more comprehensive evaluation. Greater values signify increased activity and clarity in the combined image. MI evaluates the amount of recovered information by comparing the intensity distributions in the source image pair. MSSIM measures the amount of distortion in the composite image, whereas QAB/F evaluates the edge information preserved from the source images, which is particularly crucial in clinical image fusion for accurate pathology assessments. Higher QAB/F values indicate better integration of edge characteristics, texture, and bone structures. A statistical examination of the testing results shows that the proposed algorithm performs significantly better than existing methods. Standard deviation rises from 15.5 to 32.7%, spatial frequency from 38.2 to 70.5%, mutual information from 42.8 to 62.9%, edge

Table 1. Description of image quality assessment metrics.

Performance Metric	Mathematical formulae
Average Pixel Intensity (API)	For an image $f(i,j)$ of size MXN, $\text{API} = \frac{1}{MN}\sum_{i=1}^{M}\sum_{j=1}^{N} f(i,j)$ Higher value of API produces an image with more contrast.
Standard Deviation (SD)	It is a metric for the level of deviation in a mean collection of image data. $SD = \sqrt{\frac{1}{MN}\sum_{i-1}^{M}\sum_{j=1}^{N}(f(i,j)-\text{API})^2}$
Entropy (H)	It estimates information content in an image. Large value of H indicates an image with more information. For an image with probability of pixel intensity distribution P_k, entropy is calculated as follows: $H = -\sum_{k=0}^{255} P_k \log(P_k)$
Mutual Information (MI)	For two source images A, B and fused image F, Mutual information is given as $\text{MI}_F^{AB} = \text{MI}(A,F) + \text{MI}(B,F)$ $\text{MI}(A,F) = \sum_{z\in Z}\sum_{y\in Y} p(A,F)\log_2 \frac{p(A,F)}{p(A)p(F)}$ $\text{MI}(B,F) = \sum_{z\in Z}\sum_{y\in Y} p(B,F)\log_2 \frac{p(B,F)}{p(B)p(F)}$ The quantity of activity level data that is transmitted from the source images into the fused image is measured.
Spatial Frequency (SF)	It measures an resolution level of an image. Higher value is desired. $\text{SF}(i,j) = \sqrt{\|\text{RF}(i,j)\|^2 + \|\text{CF}(i,j)\|^2}$ $\text{RF}(i,j) = \sqrt{\frac{1}{MN}\sum_{i=2}^{M}\sum_{j=2}^{N}[I(i,j)-I(i,j-1)]^2}$ $\text{CF}(i,j) = \sqrt{\frac{1}{MN}\sum_{i=2}^{M}\sum_{j=2}^{N}[I(i,j)-I(i-1,j)]^2}$
Edge strength (Q_{ABF})	Q_{ABF} represents the degree to which the edge information from the input images transitions into the fused image. The evaluation is as follows: $Q_{ABF} = \frac{\sum_{i=1}^{M}\sum_{j=1}^{N}(Q_{AF}(i,j)W_A(i,j)+Q_{BF}(i,j)W_B(i,j))}{\sum_{i=1}^{M}\sum_{j=1}^{N}(W_A(i,j)+W_B(i,j))}$
Mean Structural Similarity Index Measure (MSSIM)	$\text{SSIM}(A,F) = \frac{(2\mu_A\mu_F+C1)(2\sigma_{AF}+C2)}{(\mu_A^2+\mu_F^2+C1)(\sigma_A^2+\sigma_F^2+C2)}$ Where μ_A is the mean of A and μ_F is the mean of F, σ_{AF} is the covariance of A and F, σ_A^2 is the variance of A, and σ_F^2 is the variance of F. To avoid instability that can result from a division with a value near to zero, two constants, $C1$ and $C2$, are used. SSIM readings can range from 0 to 1, with 0 signifying poor quality and 1 signifying excellent quality. A higher MSSIM score results in less distortion within the fused image. $\text{MSSIM} = \frac{\text{SSIM}(A,F)+\text{SSIM}(B,F)}{2}$

Table 2. Statistical evaluations of the suggested approach for multimodal data.

| Dataset type	Method	Standard Deviation (SD)	Mutual Information (MI)	Spatial Frequency (SF)	Image entropy (H)	Edge strength (QAB/F)	MSSIM
Dataset-I	SR	30.82	2.57	11.68	5.80	0.5756	0.5122
	DWT	44.71	1.92	17.13	6.17	0.6073	0.5246
	NSST	44.16	2.05	17.05	6.20	0.6816	0.5366
	CNN	52.89	2.43	17.40	6.07	0.7184	0.5518
	Guided filter (GF)	52.89	2.31	16.97	6.52	0.7210	0.5634
	Proposed	58.29	5.68	20.42	6.79	0.8460	0.9949
Dataset-II	SR	51.40	3.42	17.76	4.94	0.5178	0.8248
	DWT	55.73	3.19	22.01	5.19	0.5051	0.7915
	NSST	54.56	3.34	20.95	5.12	0.5887	0.8160
	CNN	59.92	3.34	21.93	4.89	0.5888	0.8146
	Guided filter (GF)	55.68	3.79	20.25	5.20	0.6028	0.8207
	Proposed	63.12	4.72	36.85	5.90	0.8250	0.9961
Dataset-III	SR	61.50	3.18	20.19	4.52	0.5157	0.7640
	DWT	66.53	3.12	25.11	4.86	0.5473	0.7489
	NSST	65.89	3.20	24.52	4.88	0.5971	0.7733
	CNN	69.60	3.38	25.99	4.39	0.6042	0.7775
	Guided filter (GF)	69.63	3.34	24.39	5.05	0.6119	0.7762
	Proposed	73.53	4.45	35.14	5.83	0.8089	0.9929
Dataset-IV	SR	69.84	3.33	28.98	7.56	0.4964	0.6532
	DWT	76.80	3.08	35.94	7.41	0.4699	0.6263
	NSST	79.49	3.23	34.60	7.44	0.5349	0.6628
	CNN	79.84	3.26	32.85	7.31	0.5171	0.6462
	Guided filter (GF)	75.36	3.52	34.30	7.60	0.5510	0.6602
	Proposed	90.15	5.43	50.54	7.93	0.8727	0.9945
Dataset-V	SR	51.71	3.19	17.58	5.24	0.4823	0.7427
	DWT	55.72	2.80	22.28	5.36	0.4573	0.7098
	NSST	53.79	2.94	21.47	5.44	0.5226	0.7311
	CNN	61.11	3.18	23.06	4.83	0.5214	0.7448
	Guided filter (GF)	66.98	3.23	21.56	5.60	0.5330	0.7342
	Proposed	81.63	4.67	37.27	6.01	0.8711	0.9927
Dataset-VI (MR-SPECT)	SR	47.02	4.02	18.86	4.21	0.6056	0.7617
	DWT	41.36	3.37	18.74	3.63	0.5783	0.7239
	NSST	48.53	4.07	19.28	4.13	0.7120	0.7451
	CNN	45.82	3.86	20.06	4.04	0.7248	0.7604
	Guided filter (GF)	41.27	3.65	18.56	3.77	0.6761	0.7462
	Proposed	58.19	4.67	24.86	4.43	0.9023	0.9940
Dataset-VII (MR-PET)	SR	63.45	4.65	22.19	5.18	0.5660	0.7572
	DWT	58.61	3.91	23.11	4.43	0.5371	0.7189
	NSST	68.94	4.32	24.52	4.98	0.6708	0.7411
	CNN	62.47	4.17	27.96	4.76	0.6836	0.7584
	Guided filter (GF)	58.26	3.97	24.39	4.45	0.6449	0.7432
	Proposed	73.99	5.19	28.87	5.88	0.8595	0.9987
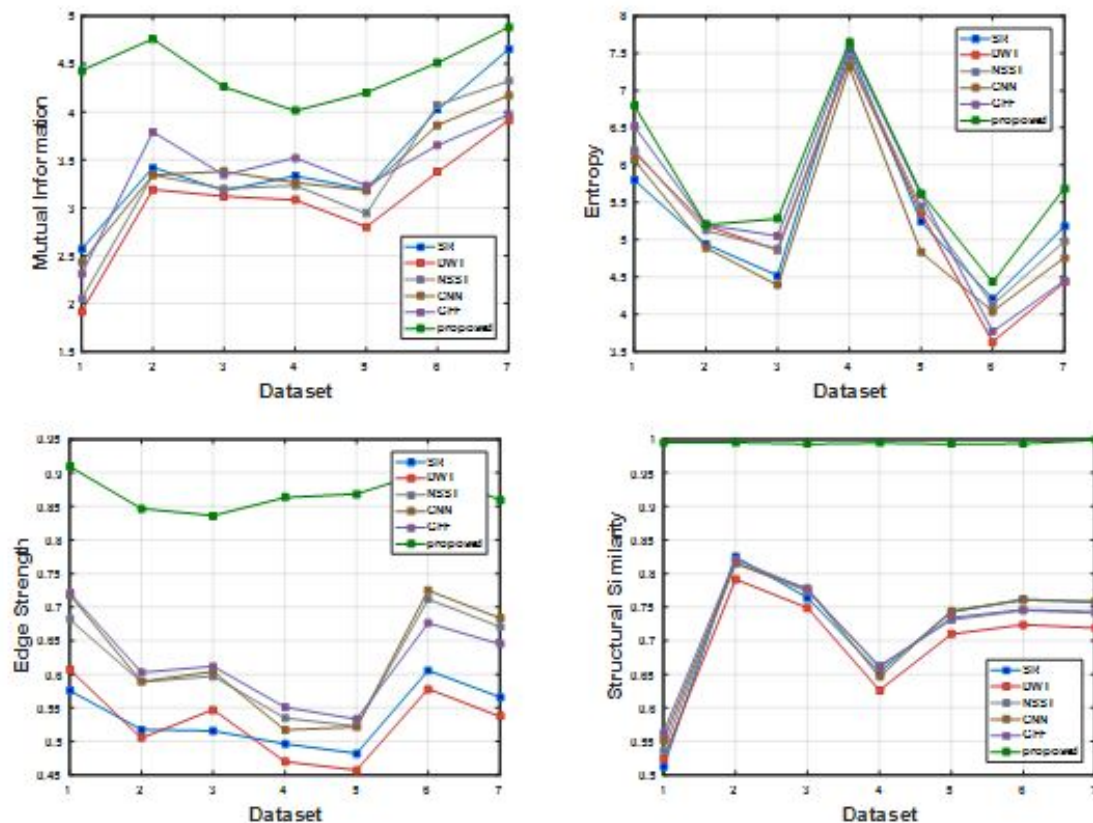
Figure 13. Comparative analysis of average value of quality assessment metrics.

strength from 37.4 to 61.9%, structural similarity index from 37.8 to 43.8%, and image entropy from 12 to 18%. These improvements demonstrate that the combined image has minimal distortion and that crucial edges, soft tissues, dense structures, and features are successfully maintained.

5. Conclusion

A new fusion method for MRI and CT medical images is presented in this paper by decomposing the source images into base and detail layers through proposed three scale decomposition and fusing the base layers based on grey optimization algorithm with maximization of entropy, edge strength and standard deviation as objective function while fusing the detail layers based on enhanced dual channel PCNN. Comprehensive contrast experiments have been carried out on many pairs of CT and MR images together with SPECT and PET images, proving that the proposed method is superior in both qualitative and objective assessment. Therefore recommended technique is more effective in aiding medical professionals in making accurate disease diagnoses.

References

[1] X. Liu, W. Mei, and H. Du. "**Multi-modality medical image fusion based on image decomposition framework and nonsubsampled shearlet transform**.". *Biomed. Signal Process. Control*, 40:343–350, 2018.
DOI: https://doi.org/10.1016/j.bspc.2017.10.001.

[2] Z. Ding, D. Zhou, R. Nie, R. Hou, and Y. Liu. "**Brain medical image fusion based on dual-branch CNNs in NSST domain**.". *BioMed Res. Int.*, 2020:1–15, 2020.
DOI: https://doi.org/10.1155/2020/6265708.

[3] Z. Zhu, M. Zheng, G. Qi, D. Wang, and Y. Xiang. "**A phase congruency and local laplacian energy based multi-modality medical image fusion method in NSCT domain**.". *IEEE Access*, 7:20811–20824, 2019.
DOI: https://doi.org/10.1109/access.2019.2898111.

[4] S. Wang and Y. Shen. "**Multi-modal image fusion based on saliency guided in NSCT domain**.". *IET Image Process.*, 2020.
DOI: https://doi.org/10.1049/iet-ipr.2019.1319.

[5] Y. Yang. "**A novel DWT based multi-focus image fusion method**.". *Proc. Eng.*, 24:177–181, 2011. DOI: https://doi.org/10.1016/j.proeng.2011.11.2622.

[6] B. Yu, B. Jia, L. Ding, Z. Cai, Q. Wu, R. Law, J. Huang, L. Song, and S. Fu. "**Hybrid dual-tree complex wavelet transform and support vector machine for digital multi-focus image fusion**.". *Neurocomputing*, 182:1–9, 2016. DOI: https://doi.org/10.1016/j.neucom.2015.10.084.

[7] J. Du, W. Li, B. Xiao, and Q. Nawaz. "**Union laplacian pyramid with multiple features for medical image fusion**.". *Neurocomputing*, 194:326–339, 2016. DOI: https://doi.org/10.1016/j.neucom.2016.02.047.

[8] J. Fu, W. Li, J. Du, and B. Xiao. "**Multimodal medical image fusion via laplacian pyramid and convolutional neural network reconstruction with local gradient energy strategy**.". *Comput. Biol. Med.*, 126:104048, 2020. DOI: https://doi.org/10.1016/j.compbiomed.2020.104048.

[9] Y. Liu, X. Chen, R.K. Ward, and Z.J. Wang. "**Image fusion with convolutional sparse representation**.". *IEEE Signal Process. Lett.*, 23(12):1882–1886, 2016. DOI: https://doi.org/10.1109/lsp.2016.2618776.

[10] S. Li, X. Kang, and J. Hu. "**Image Fusion With Guided Filtering**.". *IEEE Trans. Image Process.*, 22(7):2864–2875, 2013. DOI: https://doi.org/10.1109/TIP.2013.2244222.

[11] Q. Zhang, X. Shen, L. Xu, and J. Jia. "**Rolling Guidance Filter**.". *Lect. Notes Comput. Sci.*, 8691:1–16, 2014. DOI: https://doi.org/10.1007/978-3-319-10578-9_53.

[12] W. Tan, J. Zhang, P. Xiang, H. Zhou, and W. Thitøn. "**Infrared and visible image fusion via NSST and PCNN in multiscale morphological gradient domain**.". *Proc. SPIE*, 2020. DOI: https://doi.org/10.1117/12.2551830.

[13] M. Yin, X. Liu, Y. Liu, and X. Chen. "**Medical Image Fusion With Parameter-Adaptive Pulse Coupled Neural Network in Nonsubsampled Shearlet Transform Domain**.". *IEEE Trans. Instrum. Meas.*, 68(1):49–64, 2019. DOI: https://doi.org/10.1109/TIM.2018.2838778.

[14] A. Vaswani. "**Attention is all you need**.". *Adv. Neural Inf. Process. Syst.*, 30:5998–6008, 2017. DOI: https://doi.org/10.48550/arXiv.1706.03762.

[15] X. Xie, X. Zhang, S. Ye, D. Xiong, L. Ouyang, and B. Yang. "**MRSCFusion: joint residual swin transformer and multiscale CNN for unsupervised multimodal medical image fusion**.". *IEEE Trans. Instrum. Meas.*, 72:1–17, 2023. DOI: https://doi.org/10.1109/TIM.2023.3317470.

[16] Z. Zhao, H. Bai, J. Zhang, Y. Zhang, S. Xu, and Z. Lin. "**CDDFuse: correlation-driven dual-branch feature decomposition for multimodality image fusion**.". *Proc. IEEE/CVF Conf. Comput. Vis. Pattern Recognit.*, pages 5906–5916, 2023. DOI: https://doi.org/10.48550/arXiv.2211.14461.

[17] X. Xu, D. Shan, G. Wang, and X. Jiang. "**Multimodal medical image fusion using PCNN optimized by the QPSO algorithm**.". *Appl. Soft Comput.*, 46:588–595, 2016. DOI: https://doi.org/10.1016/j.asoc.2016.03.028.

[18] H. M. El-Hoseny, W. A. El-Rahman, E.-S. M. El-Rabaie, F. E. Abd El-Samie, and O. S. Faragallah. "**An efficient DT-CWT medical image fusion system based on modified central force optimization and histogram matching**.". *Infrared Phys. Technol.*, 94:223–231, 2018. DOI: https://doi.org/10.1016/j.infrared.2018.09.003.

[19] E. Daniel, J. Anitha, K. K. Kamaleshwaran, and I. Rani. "**Optimum spectrum mask based medical image fusion using Gray Wolf Optimization**.". *Biomed. Signal Process. Control*, 34:36–43, 2017. DOI: https://doi.org/10.1016/j.bspc.2017.01.003.

[20] C. S. Asha, S. Lal, V. P. Gurupur, and P. U. P. Saxena. "**Multi-Modal Medical Image Fusion With Adaptive Weighted Combination of NSST Bands Using Chaotic Grey Wolf Optimization**.". *IEEE Access*, 7:40782–40796, 2019. DOI: https://doi.org/10.1109/ACCESS.2019.2908076.

[21] E. Daniel. "**Optimum Wavelet-Based Homomorphic Medical Image Fusion Using Hybrid Genetic–Grey Wolf Optimization Algorithm**.". *IEEE Sensors J.*, 18(16):6804–6811, 2018. DOI: https://doi.org/10.1109/JSEN.2018.2822712.

[22] Parvathy, V. Subbiah, and S. Pothiraj. "**Multi-modality medical image fusion using hybridization of binary crow search optimization**.". *Health Care Manag. Sci.*, 23:661–669, 2020. DOI: https://doi.org/10.1007/s10729-019-09492-2.

[23] K. Padmavathi, C. S. Asha, and V. K. Maya. "**A novel medical image fusion by combining TV-L1 decomposed textures based on adaptive weighting scheme**.". *Eng. Sci. Technol., Int. J.*, 23(1):225–239, 2020. DOI: https://doi.org/10.1016/j.jestch.2019.03.008.

[24] T. Akbarpour et al. "**Fusion of multimodal medical images using nonsubsampled shearlet transform and particle swarm optimization**.". *Multidimens. Syst. Signal Process.*, 31:269–287, 2020. DOI: https://doi.org/10.1007/s11045-019-00662-7.

[25] L. Xu, Y. Si, S. Jiang, Y. Sun, and H. Ebrahimian. "**Medical image fusion using a modified shark smell optimization algorithm and hybrid wavelet-homomorphic filter**.". *Biomed. Signal Process. Control*, 59:101885, 2020. DOI: https://doi.org/10.1016/j.bspc.2020.101885.

[26] J. Du, M. Fang, Y. Yu, and G. Lu. "**An adaptive two-scale biomedical image fusion method with statistical comparisons**.". *Comput. Methods Programs Biomed.*, 196:105603, 2020. DOI: https://doi.org/10.1016/j.cmpb.2020.105603.

[27] Y. Liu, X. Chen, R. K. Ward, and Z. J. Wang. "**Image fusion with convolutional sparse representation**.". *IEEE Signal Process. Lett.*, 23(12):1882–1886, 2016. DOI: https://doi.org/10.1109/LSP.2016.2618776.

[28] Y. Liu, X. Chen, R. K. Ward, and Z. J. Wang. "**Medical image fusion via convolutional sparsity based morphological component analysis**.". *IEEE Signal Process. Lett.*, 26(3):485–489, 2019. DOI: https://doi.org/10.1109/LSP.2019.2895749.

[29] S. Maqsood and U. Javed. "**Multi-modal Medical Image Fusion based on Two-Scale Image Decomposition and Sparse Representation**.". *Biomed. Signal Process. Control*, 57:101810, 2020. DOI: https://doi.org/10.1016/j.bspc.2019.101810.

[30] C. Pei, K. Fan, and W. Wang. "**Two-Scale Multimodal Medical Image Fusion Based on Guided Filtering and Sparse Representation**.". *IEEE Access*, 8:140216–140233, 2020. DOI: https://doi.org/10.1109/ACCESS.2020.3013027.

[31] N. Amini, E. Fatemizadeh, and H. Behnam. "**MRI-PET image fusion based on NSCT transform using local energy and local variance fusion rules**.". *J. Med. Eng. Technol.*, 38(4):211–219, 2014. DOI: https://doi.org/10.3109/03091902.2014.904014.

[32] M. Sumathi and R. Barani. "**Qualitative Evaluation of Pixel-level Image Fusion Algorithms**.". *Proc. Int. Conf. Pattern Recognit. Inform. Med. Eng.*, 2012. DOI: https://doi.org/10.1109/ICPRIME.2012.6208364.

[33] M. Yin, X. Liu, Y. Liu, and X. Chen. "**Medical Image Fusion With Parameter-Adaptive Pulse Coupled Neural Network in Nonsubsampled Shearlet Transform Domain**.". *IEEE Trans. Instrum. Meas.*, 68(1):49–64, 2019. DOI: https://doi.org/10.1109/TIM.2018.2838778.

[34] S. Mirjalili, S. M. Mirjalili, and A. Lewis. "**Grey wolf optimizer**.". *Adv. Eng. Softw.*, 69:46–61, 2014. DOI: https://doi.org/10.1016/j.advengsoft.2013.12.007.

[35] M. Yin, X. Liu, Y. Liu, and X. Chen. "**Medical image fusion with parameter adaptive pulse coupled neural network in nonsubsampled shearlet transform domain**.". *IEEE Trans. Instrum. Meas.*, 68 (1):49–64, 2019.
DOI: https://doi.org/10.1109/TIM.2018.2838778.

[36] S. Liu, J. Wang, Y. Lu, H. Li, J. Zhao, and Z. Zhu. "**Multi-focus image fusion based on adaptive dual-channel spiking cortical model in non-subsampled shearlet domain**.". *IEEE Access*, 7: 56367–56388, 2019.
DOI: https://doi.org/10.1109/ACCESS.2019.2900376.

[37] Z. Wang, S. Wang, and L. Guo. "**Novel multi-focus image fusion based on PCNN and random walks**.". *Neural Comput. Appl.*, 29:

1101–1114, 2018.
DOI: https://doi.org/10.1007/s00521-016-2633-9.

[38] K. He, D. Zhou, X. Zhang, and R. Nie. "**Multi-focus: focused region finding and multi-scale transform for image fusion**.". *Neurocomputing*, 320:157–170, 2018.
DOI: https://doi.org/10.1016/j.neucom.2018.09.018.

[39] K. A. Johnson and J. A. Becker. "**The whole brain atlas**.". *Harvard Med. Sch.*, 1999. URL https://www.med.harvard.edu/aanlib/.

[40] M. V. Srikanth, A. S. Kumar, B. Nagasirisha, and T. V. Lakshmi. "**Brain MRI and CT Image Fusion Using Multiscale Local Extrema and Image Statistics**.". *ECTI-EEC*, 22(1), 2024.
DOI: https://doi.org/10.37936/ecti-eec.2024221.249146.